Hindawi
Journal of Nanomaterials
Volume 2022, Article ID 1458442, 14 pages
https://doi.org/10.1155/2022/1458442

Research Article

Efficient Removal of Cd (II) from Aquatic Media by Heteronanostructure $MgO@TiO_2@g\text{-}C_3N_4$

A. Modwi,[1] **M. Ismail**,[1] **H. Idriss**,[2] **M. A. Ben Aissa**,[1] **L. Khezami**,[3] **and M. Bououdina**[4]

[1]*Department of Chemistry, College of Science and Arts, Qassim University, Ar Rass, Saudi Arabia*
[2]*Physics Department, College of Science, Imam Mohammad Ibn Saud Islamic University (IMSIU), Riyadh 11623, Saudi Arabia*
[3]*Chemistry Department, College of Science, Imam Mohammad Ibn Saud Islamic University (IMSIU), Riyadh 11623, Saudi Arabia*
[4]*Department of Mathematics and Science, Faculty of Humanities and Sciences, Prince Sultan University, Riyadh, Saudi Arabia*

Correspondence should be addressed to A. Modwi; abuelizkh81@gmial.com and L. Khezami; lkhezami@gmail.com

Received 12 May 2022; Accepted 15 July 2022; Published 5 August 2022

Academic Editor: Haisheng Qian

Copyright © 2022 A. Modwi et al. This is an open access article distributed under the Creative Commons Attribution License, which permits unrestricted use, distribution, and reproduction in any medium, provided the original work is properly cited.

$MgO@TiO_2@g\text{-}C_3N_4$ heteronanostructure was synthesized using a simple ultrasonication technique and assessed potentially to remove Cd (II) from aqueous environments. X-ray diffraction analysis confirms composite formation with mean crystallite size in the range of 4-17 nm while transmission electron microscopy analysis reveals nanosheet-like nanoparticles with the homogeneous elemental distribution. N_2 adsorption-desorption measurements indicate the formation of a mesoporous structure with a BET surface area of about 107 m^2/g. Fourier-transformed infrared elucidates the presence of O–H, amino groups, triazine, Mg–O, and Ti–O vibrations modes. At the same time, X-ray photoelectron spectroscopy analysis manifests the presence of Mg, O, N, Ti, and C elements. For aqueous Cd (II) ions, the $MgO@TiO_2@g\text{-}C_3N_4$ nanostructure displays a superior adsorption efficiency, reaching 99.94% Cd (II) elimination with an optimum adsorption capacity of 515.86 mg/g in a short duration of 16 min. This study demonstrates the capability of using the $MgO@TiO_2@g\text{-}C_3N_4$ nanostructure as an efficient and reusable adsorbent for the uptake of Cd (II) ions in wastewater treatment and potentially for the removal of other heavy metal ions.

1. Introduction

Over the years, heavy metals have been extensively employed in a range of manufacturing processes, including mineral extraction and tannery, metal processing, metal metallurgy, and dyeing [1]. When heavy metals are used in excess, they contribute considerably to worldwide environmental concerns. The occurrence of heavy metal in industrial wastewater poses a serious hazard to human health, animals, and ecosystem [2]. The problem is that heavy metals are resistant to degradation in nature and rapidly concentrate in organisms, raising the possibility of severe risks to human health due to biomagnification in the food chain [3]. Therefore, the elimination of heavy metals and inorganic pollutants is of vital significance to environmental and human health [4].

Cadmium pollution in industrial sewage is a serious ecological issue that threatens both humans and animals from water safety and environmental point of view [5]. Cadmium is utilized in a variety of industrial activities, including electrochemical, metallurgical processing, battery manufacturing, smelting, alloy manufacturing, and mining sewage. Furthermore, cadmium can cause severe kidney problems by impairing their ability to remove acids from the blood, also causes bones osteomalacia and osteoporosis, and is a major cause of heart disease [6]. Low levels of heavy metals such as cadmium and lead commonly occur in the soil owing to the decomposition of old materials; however, high levels of these metals are caused by anthropogenic emissions, which negatively impact the ecosystems [7].

Several conventional methods have been adopted for heavy metal remediation from aquatic environments such as membrane filtration, precipitation, reverse osmosis, ion exchange, ultrafiltration, and biosorption processes [8–10]. Nevertheless, most of these techniques are expensive and generate secondary wastes. Nonetheless, adsorption has been

utilized as a powerful and reasonable method for removing organic and inorganic pollutants from wastewater [9]. This is a cost-effective approach that also provides several advantages resulting from the large variety of adsorbents that are currently accessible. Many substances were used for this purpose including charcoal, clays, natural and artificial zeolites, and kaolinite [11, 12]. Nanomaterials are very attractive and explored on a large scale in the treatment of organic and inorganic pollutants in the aquatic system [13, 14]. Specifically, the properties of metallic oxide nanoparticles such as MgO, TiO_2, ZnO, and CuO are widely used in water purification owing to their novel physicochemical proprieties besides being tuned upon the chosen chemical composition, by doping with different materials to achieve particular requirements and applications [15–18].

On the other hand, nanocomposites play an important role in environmental remediation as scavengers of water contaminants via adsorption or ion exchange [19, 20]. Tremendous efforts have been devoted in order to obtain nanocomposites with distinctive characteristics through alloying and doping [21, 22]. Nanocomposites such as RuO_2-ZnO, MgO@g-C_3N_4, ZnO-doped TiO_2/rGO, and TiO demonstrated many interesting properties, including small particle size, porous structure, a larger surface area, and the possibility of adjusting the bandgap [23–25].

This study is aimed at producing low-cost and high-performance nanocomposite as a straightforward solution to address Cd (II) contamination issues in aquatic systems. A ternary MgO@TiO_2@g-C_3N_4 nanosorbent is prepared and assessed for the removal of Cd (II) from aqueous solution. The effectiveness of the removal parameters such as the initial Cd (II) concentration, pH, and contact time in terms of adsorption capability has been evaluated. Additionally, the adsorption isotherms and kinetic studies and recyclability have been discussed. FTIR analysis elucidates a plausible mechanism for removing Cd (II) onto MgO@TiO_2@g-C_3N_4 nanostructure surface.

2. Experimental Section

2.1. Preparation of MgO@TiO_2@g-C_3N_4 Nanostructures. The g-C_3N_4 powder was prepared through urea pyrolysis degradation. 4.5 g of urea compound was placed in a covered pot and tempered at 550°C for 120 minutes at room temperature heating rate of 10°C/min. The raw yellow g-C_3N_4 obtained was then cooled, grinded, and collected in a container. Magnesium oxide (MgO) powder was synthesized by thermal decomposition of Mg carbonate salts ($MgCO_3$) at 800°C for 60 min, whereas TiO_2 nanopowder was purchased from Sigma Aldrich.

Magnesium and titanium oxide graphitic carbon nitride nanostructure (MgO@TiO_2@g-C_3N_4) was prepared by utilizing a conventional ultrasonication process. 1.84 g of g-C_3N_4 was sonicated for 15 min in 125 mL methanol. A 400 mg of MgO and TiO_2 powdered mixture was added to the g-C_3N_4 methanolic solution and sonicated for an additional 45 min. The resulting yellowish solution was then evaporated for 24 h at 85°C. The final product MgO@TiO_2@g-C_3N_4 was annealed for 60 min at 180°C.

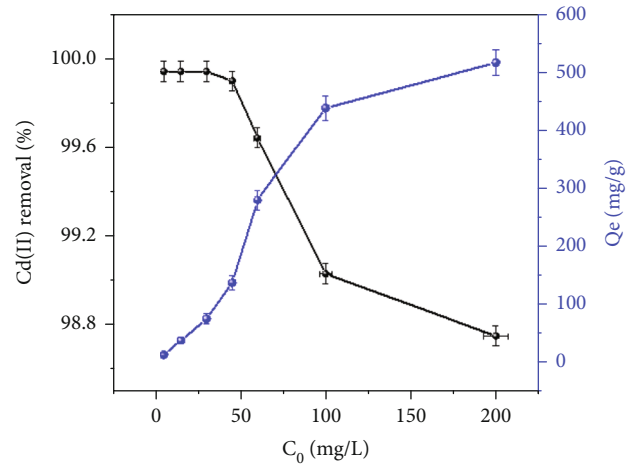

Figure 1: Variation of removal rate as function of Cd (II) initial concentration by MgO@TiO_2@g-C_3N_4 nanopowder.

2.2. Characterizations. Rigaku D/max-RA powder diffractometer equipped with Cu-Kα radiation source ($\lambda = 1.5418$ Å) was used to analyze the crystal structure and to determine structural and microstructural parameters of $MgTiO_3$@g-C_3N_4 nanopowder. The Brunauer–Emmett–Teller (BET) surface area of the nanomaterial was determined by recording N_2 adsorption/desorption at 196°C on a Micrometrics ASAP 2020 analyzer. A Hitachi H-800 transmission electron microscope (TEM) equipped with electron dispersive X-ray (EDX) spectroscopy was used for morphological observations and elemental chemical analysis. The chemical surface properties of the as-prepared nanopowder were investigated by means of X-ray photoelectron spectroscopy (XPS) using Perkin Elmer PHI 550 ESCA/SAM equipped with a monochromatized Al-Kα X-ray source ($h\nu = 1486.6$ eV) and a hemispherical electron analyzer. To elucidate the possible adsorption mechanism, Fourier-transformed infrared (FTIR) spectra of MgO@TiO_3@g-C_3N_4 nanopowder before and after Cd (II) removal were recorded by using KBr pellet technique on a Nicolet Nexus 870 FTIR spectrometer.

2.3. Cd (II) Adsorption Experiments. Batch experiments were performed to assess the adsorption isotherms of Cd (II) on MgO@TiO_3@g-C_3N_4 heteronanostructure. A 10 mg of MgO@TiO_3@g-C_3N_4 sorbent was introduced in 50 mL glass bottles with initial concentrations of the Cd (II) ranging from 5 to 200 ppm. The mixture suspensions were magnetically stirred for 1440 min. Upon attaining equilibrium with the aqueous phase, the nanopowder was centrifuged and the residual Cd (II) concentrations in the aliquot were determined by atomic absorption spectroscopy (AAS) (Hitachi Z-8100, Japan).

The amount of adsorbed Cd (II) ions at any time t (min) and subsequently the equilibrium value of q_t and q_e (in mg/g) were calculated by using the following equations:

$$q_t = \frac{V(C_0 - C_t)}{m},$$
$$q_e = \frac{V(C_0 - C_e)}{m}, \quad (1)$$

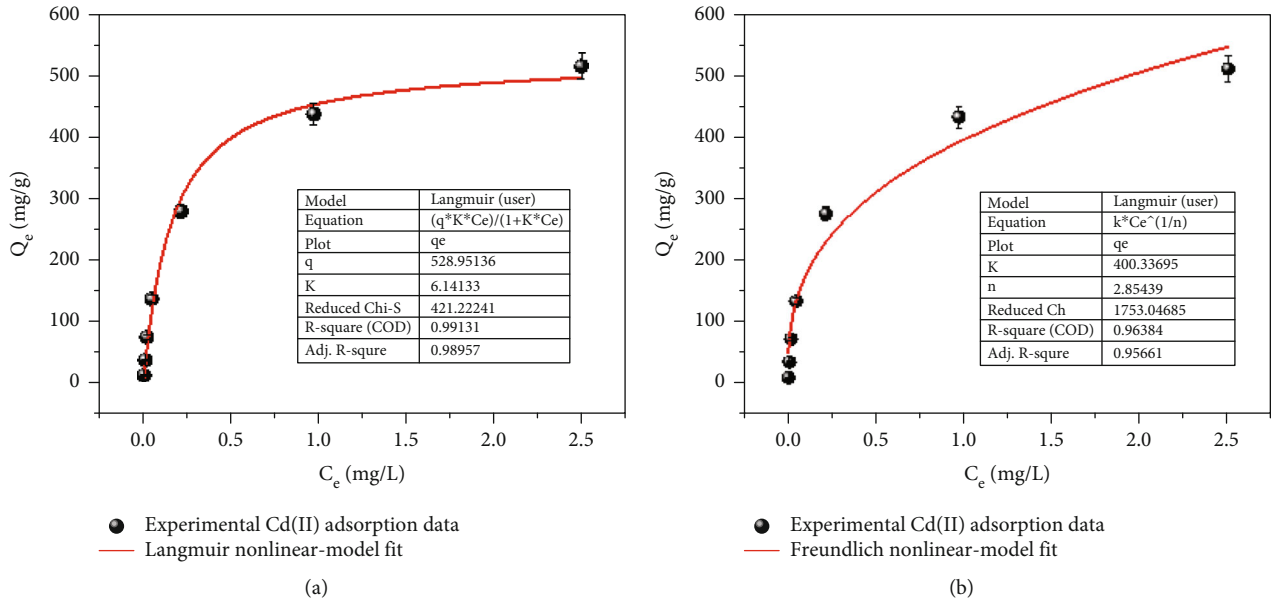

Figure 2: Experimental Cd (II) adsorption by MgO@TiO_2@g-C_3N_4 nanopowder fitted with nonlinear Langmuir and Freundlich models.

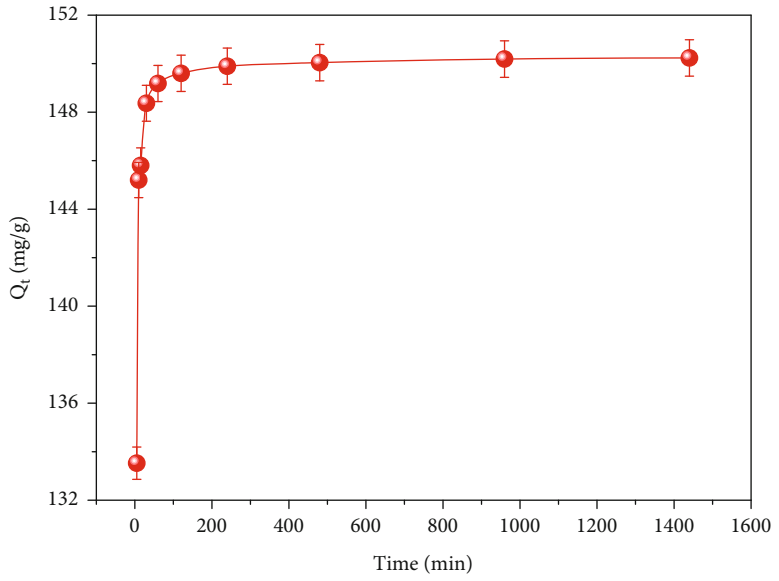

Figure 3: Effect of contact time on Cd (II) removal by MgO@TiO_2@g-C_3N_4 nanopowder.

where V is the solution volume (L), C_0, C_e, and C_t are the initial concentration, equilibrium concentration, and concentration at any time t of Cd (II) metal ions (mg/L) in solution, and m is the mass of the adsorbent (g). All the measurements were reproduced twice, and only the average values were reported in the manuscript. The ultimate attained deviation was found to be smaller than 5%. All the experimental data were plotted and modelled using the Origin 2019b software. All dynamic and equilibrium graphs were illustrated with error bars (i.e., Figures 1–4). Moreover, all statistical data obtained from Origin are presented in Table 1.

3. Results and Discussions

3.1. Characterization of MgO@TiO_3@g-C_3N_4

3.1.1. Structural Analysis. The XRD pattern of $MgTiO_3$@g-C_3N_4 nanopowder, as shown in Figure 5, displays well-defined diffraction peaks with relative broadening and intensity, manifesting the formation of well-nanocrystallized phase(s).

Peaks' identification using High Score program indicates the presence of three phases, i.e., MgO, anatase TiO_2, and g-C_3N_4. The characteristic diffraction peaks at $2\theta = 12.7^\circ$ and 27.38° for g-C_3N_4 appear to correlate with the in-plane

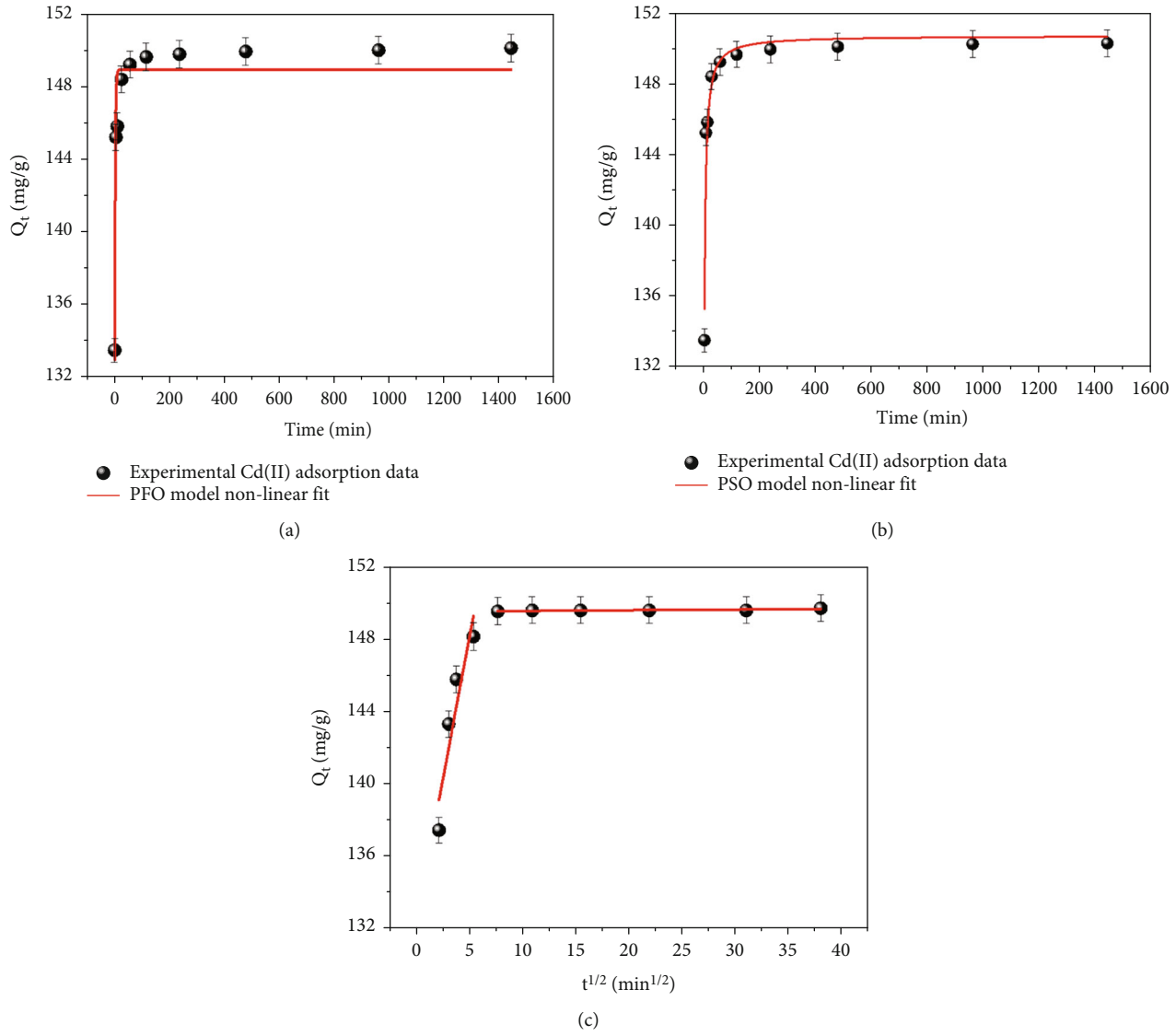

Figure 4: (a) PFO and (b) PSO kinetics; (c) IPD models for Cd (II) adsorption by MgO@TiO_2@g-C_3N_4 nanopowder.

structural packing pattern (100) and interlayer stacking plane (002) of the hexagonal structure (JCPDS card No. 87-1526) [26], whereas the peaks located at 2θ of 25.07°, 37.59°, 47.05°, 53.91°, 61.99°, 69.09, and 74.53° represent the distinctive reflections (101), (004), (200), (105), (204), (116), and (220) of the anatase phase TiO_2 (JCPDS card No. 021-1272) [27]. The remaining peaks observed at 2θ of 36.61°, 42.53°, 61.99°, and 78.16° are assigned to the MgO cubic structure's (111), (200), (220), and (222) planes [28].

The crystallite size (D) has been calculated using the well-known Scherrer equation:

$$D = \frac{K\lambda}{\beta \cos\theta}, \tag{2}$$

where K is constant depending on particle's shape ($K = 0.9$ for spherical morphology), λ is the wavelength of the X-ray source (1.5418 Å), β is the full width at half maximum of the chosen reflection (in rad), and θ is the diffraction of the chosen reflection.

For anatase TiO_2 ($I4_1$/amd, space group No. 141), MgO with rock-salt type structure (Fm-3 m, space group No. 225), and g-C_3N_4 (Fd-3 m, space group No. 227) with a tetragonal, cubic, and cubic crystal structures, respectively, the lattice parameters are calculated by means of the following equations:

$$\frac{1}{d^2} = \left(\frac{h^2 + k^2}{a^2}\right) + \frac{l^2}{c^2}, \tag{3}$$

$$\frac{1}{d^2} = \left(\frac{h^2 + k^2 + l^2}{a^2}\right), \tag{4}$$

where d is the interplanar spacing and h, k, l are Miller indices of the corresponding diffraction peak. The calculated

Table 1: Parameters calculated from kinetics models for Cd (II) adsorption onto MgO@TiO_2@g-C_3N_4 heteronanostructure.

Model name	Parameters	Variable unit	Computed values
PFO	q_e	mg/g	148.91 ± 0.5395
	k_1	L/min	0.4471 ± 0.019
	R^2	-	0.9232
PSO	$q_{e\,(calculated)}$	mg/g	150.66 ± 0.6748
	$q_{e\,(experimental)}$	mg/g	150.31 ± 0.4748
	k_2	mg/mg.min	0.01168 ± 0.0010
	R^2	-	0.9650
IPD	C_1	-	132.20 ± 3.2632
	k_{dif1}	mg/mg.min	3.118 ± 0.84255
	R^2	-	0.9341
	C_2	-	149.53 ± 0.0033
	k_{dif2}	mg/mg.min	0.0039 ± 0.00014
	R^2	-	0.8101

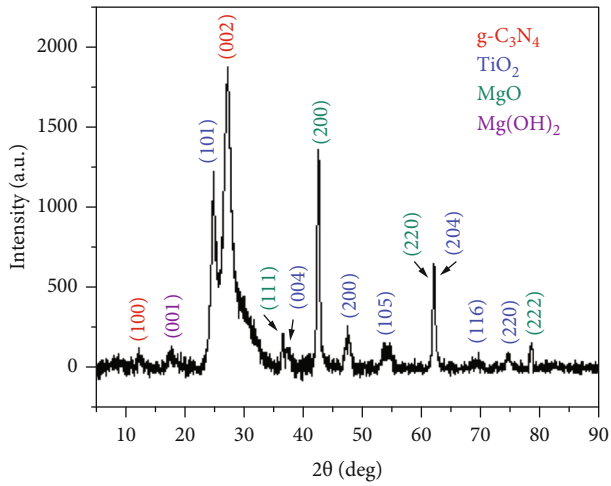

Figure 5: XRD patter of $MgTiO_3$@g-C_3N_4 nanopowder.

Table 2: Microstructural (crystallite size) and structural (lattice parameters and unit cell volume) parameters of TiO_2, MgO, and g-C_3N_4 phases.

Phases	Crystallite size (nm)	Lattice parameters (unit A (angstrom))
TiO_2	11.34	$a = 3.8196$ $c = 9.7815$
MgO	17.09	$a = 4.2424$
g-C_3N_4	4.08	$a = 6.5093$

crystallite size of the lattice parameters of TiO_2, MgO, and g-C_3N_4 phases are reported in Table 2. It can be noticed that the crystallite size for all phases is within the nanoscale regime, i.e., 4–17 nm. The as obtained heterostructured composite with high surface area would be suitable for the adsorption of heavy metal ions. The computed lattice parameters are found to deviate from the bulk compounds, i.e., 3.6600 Å and 9.7600 Å for anatase TiO_2 [29], 4.2110 Å for MgO [30], and 6.7824 Å for g-C_3N_4 [31]. This can be associated with the occurrence of the dissolution of Mg ions within TiO_2 host lattice by occupying Ti ionic sites followed by its expansion since Mg^{2+} (0.72 Å) has a larger ionic radius compared to that of Ti^{4+} (0.61 Å).

3.1.2. Morphology and Chemical Composition. As shown in Figures 6(a) and 6(b), TEM images of the synthesized MgO@TiO_2@g-C_3N_4 powder exhibit characteristic two-dimensional nanosheet-like nanoparticles with a corrugated thickness of around 27 nm. As can be seen, the integrated MgO and TiO_2 nanoparticles in the MgO@TiO_2@g-C_3N_4 nanostructure have an average particle size of about 20-50 nm. The EDX spectrum (Figure 6(c)) displays typical characteristic peaks of Ti, Mg, N, O, and C, hence confirming the purity of the prepared composite. The inset table in Figure 6(c) indicates the corresponding chemical composition of the synthesized MgO@TiO_2@g-C_3N_4. Furthermore, the elemental mapping of C, N, O, Mg, and Ti, as shown in Figures 6(e)–6(i), clearly evidenced the homogeneous distribution of the elements over the analyzed particles (Figure 6(d)).

3.1.3. BET Analysis. A good adsorbent, for instance MgO@TiO_3@g-C_3N_4 nanostructure, must have a significant number of available adsorption sites. In other words, the material's surface area, pore volume, and size should be enough. The nitrogen adsorption-desorption analysis (Figure 7 inset pore size) reveals that MgO@TiO_2@g-C_3N_4 nanostructure is a mesoporous material with an IUPAC type IV adsorption isotherm. The isotherm is coupled with a hysteresis of type H1, implying a restricted distribution of uniform mesoporous and limited networking effects [32, 33]. The TEM image (Figure 7) confirms the presence of pores besides the appearance of large aggregates generated by the interconnection of MgO and TiO_2 nanoparticles with g-C_3N_4 nanosheets. The surface area, total porous volume, and average pore size of MgO@TiO_2@g-C_3N_4 nanostructure are 107 m^2/g, 0.254 cc/g, and 1.57 nm, respectively. With a large surface area and porosity, the adsorbent is predicted to expose a vast number of adsorption sites, resulting in a high adsorption capacity.

3.1.4. XPS Analysis. XPS analysis is used to determine the chemical composition and the valences of the elements on the nanoadsorbent surface. Figures 8(a)–8(f) depict the XPS survey results for MgO@TiO_2@g-C_3N_4, and Mg, O, N, Ti, and C elements are detected in the whole XPS scan spectrum. The XPS spectrum of Mg-2p (Figure 8(b)) displays a single peak at 51 eV characteristic of MgO compound [34]. The XPS spectrum of O-1s (Figure 8(c)) manifests a single peak at 532 eV associated to O-1s [35, 36]. For the XPS spectrum of N-1s (Figure 8(d)), two peaks are detected, i.e., for the amino groups (401 eV) and bridging N atoms (399 eV) [37]. Similarly, the XPS spectrum of Ti-2p (Figure 8(e)) displays two peaks at 459 and 464.3 eV, corresponding to the characteristic peaks of Ti-2p3/2 and Ti-2p1/

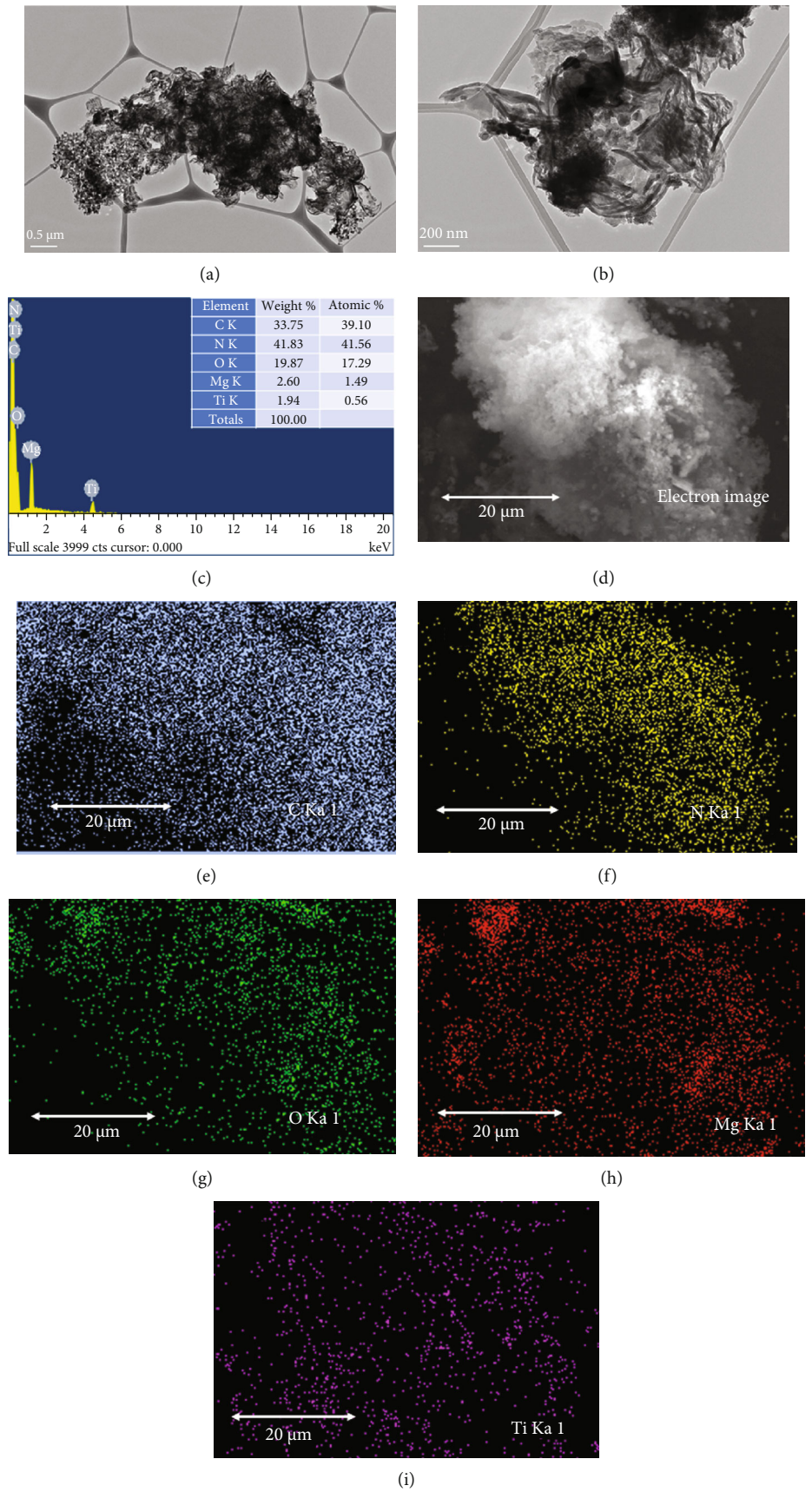

FIGURE 6: TEM images of MgO@TiO_2@g-C_3N_4 nanopowder with (a, b) different magnification, (c) EDX for element composition, and (d–i) elemental mapping of C, N, O, Mg, and Ti, respectively.

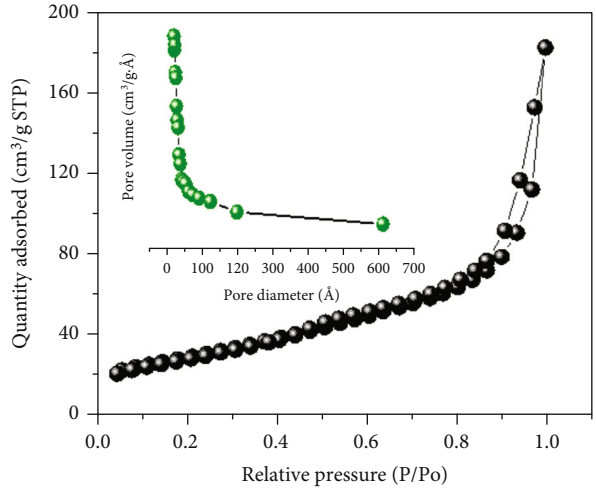

FIGURE 7: N_2 adsorption/desorption isotherm (inset pore size) for MgO@TiO_2@g-C_3N_4 nanopowder.

2, respectively [38]. Further, three peaks located at 285, 287, and 289 eV are observed in the C-1s XPS spectrum (Figure 8(f)) and attributed to C=C, C–C, and O–C bands, respectively [39]. It is clearly observed from the above XPS analysis that only Mg, Ti, C, N, and O, elements are present, thereby no presence of any impurity within the as-fabricated MgO@TiO_2@g-C_3N_4 composite.

3.2. Adsorption Ability of MgO@TiO_2@g-C_3N_4 Nanocomposite

3.2.1. Influence of Initial Cd (II) Concentration. The impact of Cd (II) concentration has been tested in the range (5–200 mg/L) under the optimized operational parameters, i.e., MgO@TiO_3@g-C_3N_4 dose (10 mg), pH 7, a fixed volume of Cd (II) solution (25 mL), at room temperature, for a contact time of 24 hrs. The percentage and the optimum adsorption capacity of Cd (II) onto MgO@TiO_3@g-C_3N_4 sorbent are shown in Figure 1. It can be observed that as the Cd (II) concentration increases, the adsorbed quantity increases gradually from 12.49 to 515.86 mg/g and the removal percentage remains very high within the range 99.94-98.75%. In this case, the fundamental driving force that increases the initial concentration of Cd (II) overcomes any barrier to Cd (II) migration from the solution. The resulting fractional adsorption becomes concentration-dependent.

3.2.2. Adsorption Isotherms Modeling. The adsorption isotherm of Cd (II) onto MgO@TiO_2@g-C_3N_4 nanopowder has been examined by introducing a certain amount of the adsorbent (dose of 400 mg/L) to the Cd (II) solution (5 to 200 mg/L) for a duration of 1440 min at room temperature and pH 7 (see Figure 2). The equilibrium concentration of Cd (II) is found to be 0.033 mg/L compared to the initial concentration of 5 mg/L, resulting in a removal efficiency greater than 99.34%. This finding indicates that MgO@TiO_2@g-C_3N_4 is an excellent adsorbent for Cd (II) removal.

To determine the adsorption behavior of the adsorbent, the experimental data has been plotted using the Freundlich (Equation (5)) and Langmuir (Equation (6)) mathematical equations:

$$q_e = K_F C_e^{1/n}, \tag{5}$$

$$q_e = \frac{Q_{\max} K_L C_e}{1 + K_L C_e}. \tag{6}$$

The constants K and n of the Freundlich model can be related to the strength of the adsorptive bond and the bond distribution, respectively [37]. In the Langmuir model (Eq. (3)), $q_{\max}$ is the solid-phase concentration corresponding to the complete monolayer coverage of adsorption sites [38]. K_L is the constant related to the free energy of adsorption. The Langmuir isotherm is the quickest, easiest, and the most effective isotherm for describing the chemical adsorption process because it is based on the following assumptions: the adsorbent configuration is homogeneous; the adsorbed molecules or atoms are held in discrete and fixed locations; each site can compensate only one molecule or atom; the energy of adsorption is consistent across all sites; and no interaction between neighboring adsorbent surface and adsorbed molecules occurs. In comparison, the Freundlich model addresses heterogeneous systems and reversible adsorption, whereas the monolayer adsorption is not restricted. Figures 2(a) and 2(b) depict linear plots of experimental data generated using the Langmuir and Freundlich models. The Langmuir model fits the data better, with a regression coefficient $R^2 = 0.991$, compared to the Freundlich model's $R^2 = 0.963$. According to the Langmuir model, the maximum adsorption capacity of the studied MgO@TiO_2@g-C_3N_4 is found to be 529 mg/g. This relatively high capacity can be attributed to its enhanced surface area and porous nanostructure with relatively large pore size. This result elucidates that Cd (II) ions are adsorbed as a monolayer over MgO@TiO_3@g-C_3N_4 surface through chemisorption being the dominant process.

3.2.3. Effect of Equilibrium Contact Duration on Cd (II) Removal. Figure 3 illustrates the effect of contact time on Cd (II) removal. The adsorption of Cd (II) ions onto the

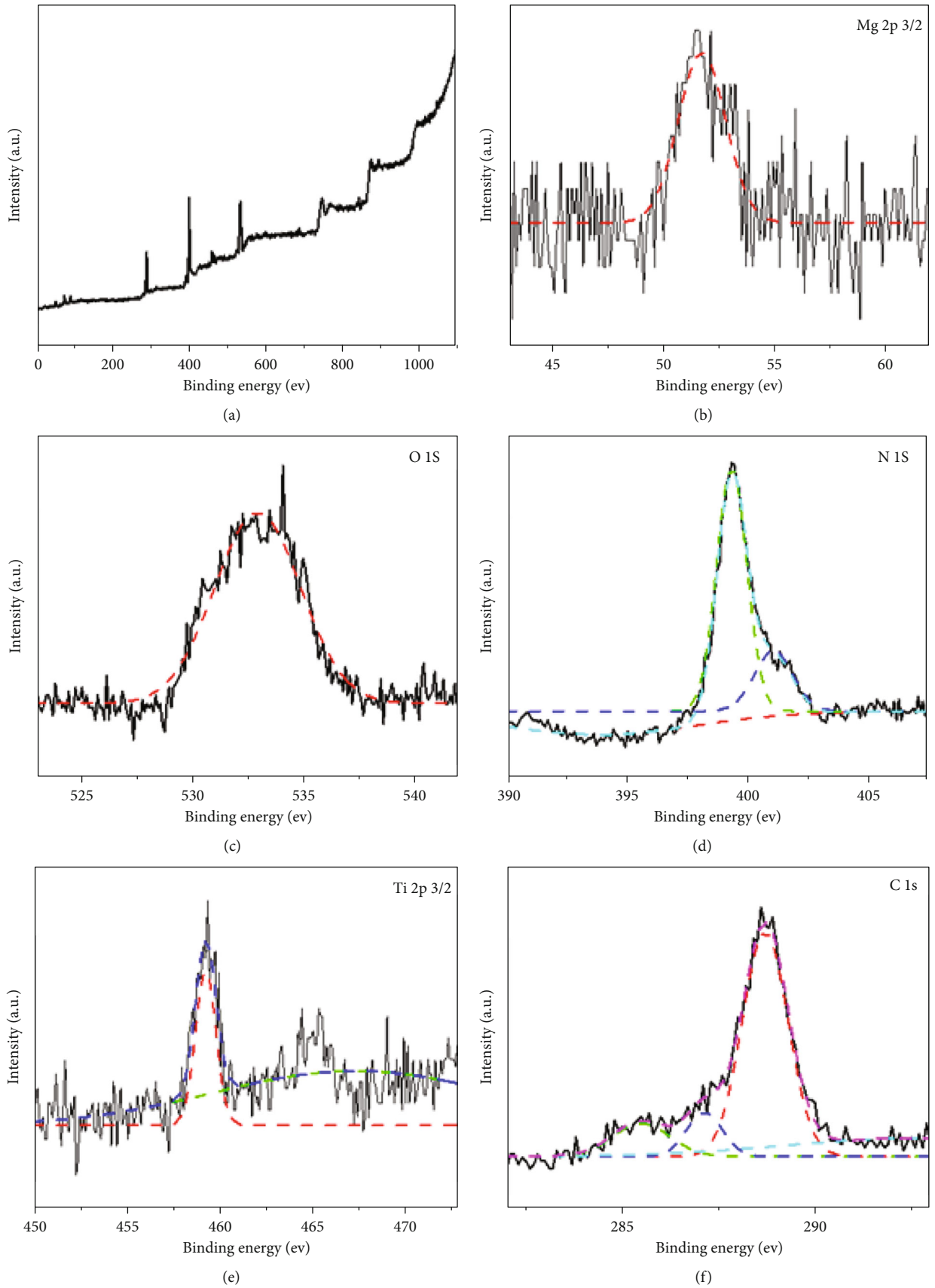

FIGURE 8: XPS spectra of (a) MgO@TiO_2@g-C_3N_4 full survey and individual spectra of (b) Mg-2p, (c) O-s, (d) N-1s, (e) Ti-2p, and (f) C-1s.

sorbent MgO@TiO_2@g-C_3N_4 nanostructure has been investigated over a stirring time in the range 5–1440 min at an initial Cd (II) concentration of 45 ppm. The removal of Cd (II) as a function of contact time approaches equilibrium in less than 16 min. Due to the numerous active sites on the sorbent MgO@TiO_2@g-C_3N_4 surface, the amount of adsorbed Cd (II) reaches approximately 150 mg/g during this short time interval. During the equilibrium period, the concentration of the active site naturally reduces, and the removal rate becomes relatively constant to reach an equilibrium state. With a large surface area and porosity, the adsorbent is predicted to expose a large number of adsorption sites, resulting in a high adsorption capacity.

3.2.4. Adsorption Kinetic Investigations. Adsorption kinetic parameters are fundamental in predicting an adsorbent's efficiency. The adsorption of Cd (II) ions onto MgO@-TiO_2@g-C_3N_4 nanostructures has been evaluated by employing pseudofirst-order (PFO), pseudosecond-order (PSO) kinetic, and intraparticle diffusion (IPD) models as displayed in Figures 4(a)–4(c). The corresponding nonlinear mathematical equations are as follows:

$$q_t = q_e\left(1 - e^{-k_1 t}\right), \tag{7}$$

$$q_t = \frac{t\,k_2 q_e^2}{k_2 q_e t + 1}, \tag{8}$$

$$q_t = k_{dif}\sqrt{t} + C. \tag{9}$$

Equation (7) describes the PFO model of Lagergren [39] with a rate constant k_1 (1/min), and q_e is the maximum amount of Cd (II) metal ions removed at equilibrium. For PSO law (Equation (8)), k_2 stands for the PSO rate constant (g/mg.min) [40]. The initial rate of sorption, $h_0 = k_2.{q_e}^2$, is assessed from PSO kinetic model equation. The half-sorption time, $t_{1/2} = 1/(k_2.q_e)$, is known as the time required for the adsorption to remove up to half as much Cd (II) metal ions as its equilibrium value.

Concerning the IPD mechanism model (Equation (9)) [41], C represents the intercept that avails more details about the thickness of the edge layer. The IPD constant, k_{dif} value (in mg/g.$min^{1/2}$), for the used adsorbent, is estimated from the slope of the plot (Figure 4(c)). The validity of these models is examined based on the regression coefficient R^2. The parameters computed from the fitting of the experimental data of Cd (II) adsorption by the kinetic models are given in Table 1. It can be noted that Cd (II) kinetic adsorption data are successfully fitted by the PSO model, since the value of $R^2 = 0.97$, implying the occurrence of Cd (II) chemisorption onto MgO@TiO_2@g-C_3N_4 nanostructures [40]. Further, the calculated value of $q_e = 150.66$ mg/g is identical to the measured value $q_e = 150.31$ mg/g. In the literature, the PSO model has recently been found to accurately predict the retention of metals on activated carbon [41].

It is known that PSO kinetic model may be used to deduce all stages of the sorption process, including exterior film diffusion, sorption, and internal particle diffusion. Nonetheless, this model cannot account for the particular adsorption mechanism [42]. Therefore, the obtained data have been analyzed using the intraparticle diffusion kinetic model (Figure 4(c)). Numerous investigations demonstrated that the intraparticle diffusion graph may exhibit multilinearity, implying the possible occurrence of two or more steps during the adsorption process [43]. The findings indicate that most data points have two straight lines, and that the plots do not cross through the origin (plots not shown).

The k_{dif2} value for MgO@TiO_2@g-C_3N_4 nanostructure is found to be lower than the k_{dif1} value, implying that intraparticle diffusion is the rate-limiting step for Cd (II) adsorption onto the hybrid composite. Also, it is important to mention that the slight deflection of the straight lines from the beginning implies that intraparticle diffusion may not be the only rate-limiting step in the adsorption of Cd (II) ions onto MgO@TiO_2@g-C_3N_4 nanostructure; other possible surface adsorption processes also contribute to the overall sorption rate [44, 45].

3.2.5. Influence of pH on Cd (II) Removal. The pH value is known to be crucial in better understanding the rate of surface reactions between adsorbate (Cd (II)) and MgO@-TiO_2@g-C_3N_4 adsorbent. The effect of pH on Cd (II) adsorption ability has been investigated in the pH range 1.0-8.0, with the optimum adsorption capacity obtained at pH 5 as shown in Figure 9. Below pH 5, significant protonation occurs on the adsorbent surface, resulting in weak adsorbate-adsorbent interactions. Similar findings were reported in analogous studies [46, 47]. Metal ions such as Cd (II) have a pH dependence on their solubility. At lower pH, Cd (II) is extremely soluble as Cd (II) free ions and $Cd(OH)^+$. Furthermore, at pH value greater than 7, Cd (II) ions will precipitate as metal hydroxide $Cd(OH)_2$ [48]. It can be concluded that the quantitative removal capacity increases with the increment of the pH solution until the pH value is equal to 7.

3.2.6. Cd (II) Adsorption Mechanism onto MgO@TiO_2@g-C_3N_4 Nanomaterial. The FTIR analysis help to clarify the adsorption mechanism of Cd (II) onto MgO@TiO_2@g-C_3N_4 nanopowder [49]. The FTIR spectra of MgO@-TiO_2@g-C_3N_4 before and after Cd (II) ions adsorption, as shown in Figure 10(a), reveal considerable changes. The O–H and the terminal amino group stretching modes situated between 3000 and 3500 cm^{-1} are shifted to lower frequencies after adsorption. Similarly, the triazine ring mode peak at 891 cm^{-1} also shifts slightly to 883 cm^{-1}. In addition, both Mg–O and Ti–O stretching vibration modes [50, 51] have mostly changed position indicating the interaction between Cd (II) and oxygen atoms of MgO@TiO_2@g-C_3N_4 by π - π stacking bridging [52]. This result indicates that functional groups of MgO@TiO_2@g-C_3N_4 (OH, CN, and N-H) and π delocalized electron systems of the triazine ring (C_3N_3) most probably are involved in the removal of Cd (II). Shen et al. reported that the triazine ring serves as a Lewis base and contributes to the Cd (II) elimination process as confirmed by FTIR and XPS analyses [53]. Based on the above FTIR observations of, a plausible sorption mechanism

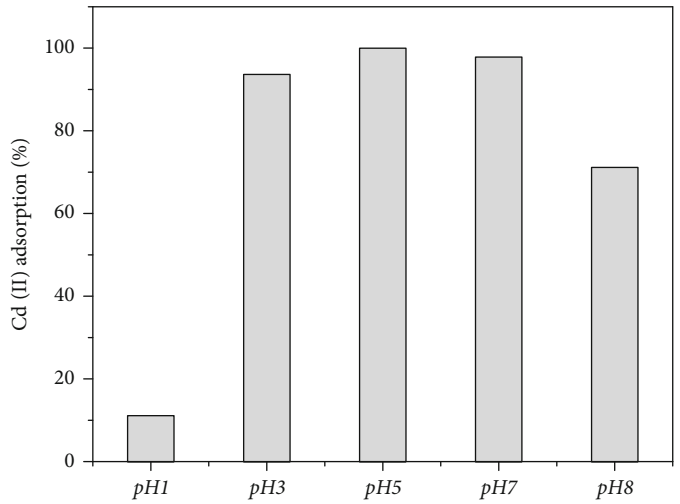

Figure 9: Effect of pH on Cd (II) removal by MgO@TiO_2@g-C_3N_4 nanopowder.

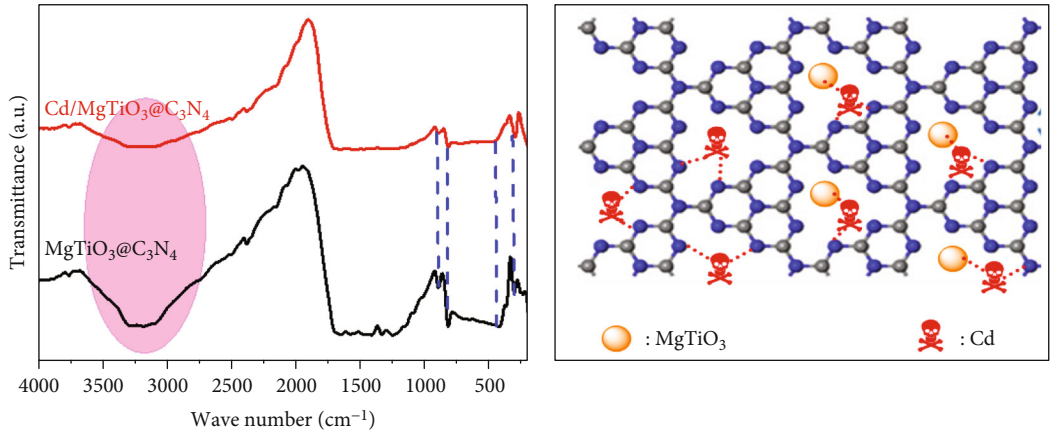

Figure 10: FTIR spectra of (a) heteronanostructure MgO@TiO_2@g-C_3N_4 before and after Cd adsorption; (b) proposed sorption mechanism.

of Cd (II) onto MgO@TiO_2@g-C_3N_4 is proposed as shown in Figure 10(b).

3.2.7. Recovery and Reusability of MgO@TiO_2@g-C_3N_4 Nanomaterial. The strategies employed to remove harmful pollutants such as heavy metal ions from diverse effluents are considered on various measures such as efficiency, suitability, stability, cost, and their reusability in large-scale industrial applications. The recycling of nanoadsorbents has become a cost-effective process. Accordingly, the regeneration of the MgO@TiO_2@g-C_3N_4 nanostructure from the reaction mixture has been investigated by adopting the same approach used by Khezami et al. [13]. In such a process, succeeding the removal process, the nanostructural material was separated from the mixture by filtration, washed with deionized water, oven-dried, and then soaked with a sodium hydroxide solution. The alkaline desorbing agent, NaOH, is proved effective in desorbing Cd (II) ions from the surface of the adsorbent. The adsorption-desorption procedure has been replicated for four consecutive cycles to test the reusability of the MgO@TiO_2@g-C_3N_4 nanostructure for the removal of Cd (II) metal ions. The below expression then estimates the metal recovery:

$$\text{Desorption efficiency\%} = \frac{\text{Amount of Cd (II) ions desorbed}}{\text{Amount of Cd (II) ions adsorbed}} \times 100\%. \quad (10)$$

As shown in Figure 11, MgO@TiO_2@g-C_3N_4 nanostructure visibly exhibits a higher constancy. It is also important to note that the synthesized heteronanostructured by a simple ultrasonication technique can be recovered and reused for four adsorption-desorption cycles.

3.3. Comparison of MgO@TiO_2@g-C_3N_4 Nanosorbent with Other Adsorbents. According to the results given in Table 3, the adsorption performance of MgO@TiO_2@g-C_3N_4 nanostructure toward aqueous Cd (II) has been further assessed in comparison to other previously adsorbents reported in the literature. Primarily, the MgO@TiO_2@g-C_3N_4 exhibits a shorter

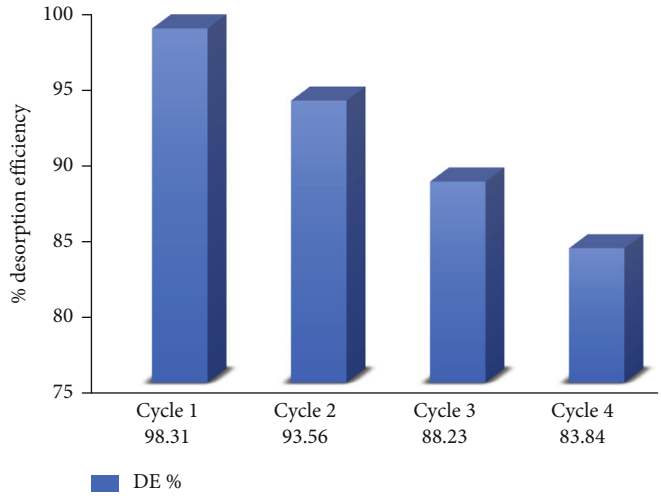

Figure 11: Desorption efficiency % of Cd (II) metal ions from MgO@TiO2@g-C3N4 nanostructure by NaOH.

Table 3: Observation parameter adsorption of the MgO@TiO_2@g-C_3N_4 compared with the various adsorbent nanomaterials.

Adsorbents	Optimal pH	Equilibrium time (min)	Removal (%)	Q_{max} (mg/g)	Refs
Date Palm Biochar	5.0	-	86.80	43.58	[45]
Fe_3O_4@SiO_2 nanoparticles	6.0	60	74.00	26.10	[54]
Phosphorus-containing iron ore	6.0	90	99.80	-	[55]
LDH@GO-SH	5.0	60	-	102.77	[56]
Silicates on diatomite	5.5	120	-	29.00	[57]
Calcium carbonate/Nano-TiO_2	5.0	8	100	103.6	[58]
Hydrated manganese dioxide	3.0	60	45.44	342.3	[59]
MgO@TiO_2@g-C_3N_4 heteronanostructure	5.0	16	99.94	515.8	This study

equilibrium duration, i.e., only 16 min, hence demonstrating rapid kinetics in the removal of Cd (II) from the aqueous solution. Further, the MgO@TiO_2@g-C_3N_4 heteronanostructure has a larger adsorption capacity compared to other nanostructures, i.e., 516 mg/g compared to 26–342 mg/g. The high performance of MgO@TiO_2@g-C_3N_4 nanosorbent for the removal of Cd (II) from aqueous solution is associated to its interesting nanostructure with a larger surface area and large pore size, making it a very promising and potentially an efficient adsorbent for the removal of other heavy metal ions.

4. Conclusion

A new mesoporous MgO@TiO_2@g-C_3N_4 nanosorbent fabricated by ultrasonication demonstrated a high adsorption capacity for the removal of Cd (II) from an aqueous solution. This was associated with its unique nanostructure composed of three main phases, high surface area, and large pore size. Furthermore, equilibrium and kinetic modelling established that the adsorption of Cd (II) ions occurred by chemisorption and is spontaneous. The FTIR analysis indicates that the functional groups of MgO@TiO_2@g-C_3N_4 (OH, CN, and N-H) and π-delocalized electron systems of the triazine ring (C_3N_3) are involved in the removal of Cd (II). This research generated mesoporous MgO@TiO_2@g-C_3N_4 heteronanostructure potentially for the removal of heavy metal ions from aqueous wastewater. The desorption studies with the concentrated NaOH method revealed that MgO@TiO_2@g-C_3N_4 nanostructure could be recovered and reused effectively.

Data Availability

The authors confirm that the data supporting the findings of this study are available within the article.

Conflicts of Interest

The authors declare that they have no known competing financial interests or personal relationships that could have appeared to influence the work reported in this paper.

Acknowledgments

The authors would like to thank the Department of Chemistry, College of Science and Arts, Al-Rass, Qassim University and Prince Sultan University for their support.

References

[1] M. K. Uddin, "A review on the adsorption of heavy metals by clay minerals, with special focus on the past decade," *Chemical Engineering Journal*, vol. 308, article S1385894716312670, pp. 438–462, 2017.

[2] P. C. Nagajyoti, K. D. Lee, and T. Sreekanth, "Heavy metals, occurrence and toxicity for plants: a review," *Environmental Chemistry Letters*, vol. 8, no. 3, article 297, pp. 199–216, 2010.

[3] O. Akpor and M. Muchie, "Remediation of heavy metals in drinking water and wastewater treatment systems: processes and applications," *International Journal of Physical Sciences*, vol. 5, no. 12, pp. 1807–1817, 2010.

[4] C. F. Carolin, P. S. Kumar, A. Saravanan, G. J. Joshiba, and M. Naushad, "Efficient techniques for the removal of toxic heavy metals from aquatic environment: a review," *Journal of Environmental Chemical Engineering*, vol. 5, no. 3, article S2213343717302208, pp. 2782–2799, 2017.

[5] F. U. Haider, C. Liqun, J. A. Coulter et al., "Cadmium toxicity in plants: impacts and remediation strategies," *Ecotoxicology and Environmental Safety*, vol. 211, article S0147651320317231, p. 111887, 2021.

[6] G. Genchi, M. S. Sinicropi, G. Lauria, A. Carocci, and A. Catalano, "The effects of cadmium toxicity," *International Journal of Environmental Research and Public Health*, vol. 17, no. 11, article ijerph17113782, p. 3782, 2020.

[7] K. Johansson, B. Bergbäck, and G. Tyler, "Impact of atmospheric long range transport of lead, mercury and cadmium on the Swedish forest environment," *Water, Air and Soil Pollution: Focus*, vol. 1, no. 3/4, article 338445, pp. 279–297, 2001.

[8] S. Gunatilake, "Methods of removing heavy metals from industrial wastewater," *Methods*, vol. 1, no. 1, 2015.

[9] D. Lakherwal, "Adsorption of heavy metals: a review," *International journal of environmental research and development*, vol. 4, no. 1, pp. 41–48, 2014.

[10] S. Saini, J. K. Gill, J. Kaur et al., "Biosorption as environmentally friendly technique for heavy metal removal from wastewater," in *Fresh water pollution dynamics and remediation*, H. Qadri, R. Bhat, M. Mehmood, and G. Dar, Eds., pp. 167–181, Springer, Singapore, 2020.

[11] S.-H. Lin and R.-S. Juang, "Adsorption of phenol and its derivatives from water using synthetic resins and low-cost natural adsorbents: a review," *Journal of Environmental Management*, vol. 90, no. 3, article S0301479708002806, pp. 1336–1349, 2009.

[12] M. Shahadat and S. Isamil, "Regeneration performance of clay-based adsorbents for the removal of industrial dyes: a review," *RSC Advances*, vol. 8, no. 43, pp. 24571–24587, 2018.

[13] L. Khezami, A. Modwi, I. Ghiloufi et al., "Effect of aluminum loading on structural and morphological characteristics of ZnO nanoparticles for heavy metal ion elimination," *Environmental Science and Pollution Research*, vol. 27, no. 3, article 7279, pp. 3086–3099, 2020.

[14] A. Modwi, K. K. Taha, L. Khezami, M. Bououdina, and A. Houas, "Silver decorated Cu/ZnO photocomposite: efficient green degradation of malachite," *Journal of Materials Science: Materials in Electronics*, vol. 30, no. 4, pp. 3629–3638, 2019.

[15] A. Modwi, B. R. Abdulkhair, M. E. Salih, N. Y. Elamin, and A. M. Fatima, "Fast and green synthesis of Sn/TiO 2 photocatalyst and it's bi-functional competence as adsorbent and photocatalyst," *Digest Journal of Nanomaterials & Biostructures (DJNB)*, vol. 14, no. 2, 2019.

[16] A. Modwi, L. Khezami, K. K. Taha, and H. Idriss, "Flower buds like MgO nanoparticles: from characterisation to indigo carmine elimination," *Zeitschrift für Naturforschung A*, vol. 73, no. 11, pp. 975–983, 2018.

[17] H. Idriss and A. Alakhras, "Clean up of malachite green dye in aqueous solution using ZnO nanopowder," *Journal of Optoelectronic and Biomedical Materials*, vol. 12, no. 4, pp. 109–119, 2020.

[18] L. Khezami, N. Elamin, A. Modwi, K. K. Taha, M. S. Amer, and M. Bououdina, "Mesoporous Sn@ TiO2 nanostructures as excellent adsorbent for Ba ions in aqueous solution," *Ceramics International*, vol. 48, no. 4, article S0272884221035471, pp. 5805–5813, 2022.

[19] A. J. Bessadok, A. Modwi, L. Khezami, K. K. Taha, and S. Mokraoui, "Physicochemical behavior of M doped Zn0. 95Cu0. 05O nanocomposites synthesized by facile sol–gel method," *Materials Research Express*, vol. 6, no. 8, article 0850g4, 2019.

[20] A. Toghan, H. M. Abd el-Lateef, K. K. Taha, and A. Modwi, "Mesoporous TiO2@ g-C3N4 composite: construction, characterization, and boosting indigo carmine dye destruction," *Diamond and Related Materials*, vol. 118, article S0925963521002545, p. 108491, 2021.

[21] A. Modwi, L. Khezami, M. G. Ghoniem et al., "Superior removal of dyes by mesoporous MgO/g-C3N4 fabricated through ultrasound method: adsorption mechanism and process modeling," *Environmental Research*, vol. 205, article S0013935121018442, p. 112543, 2022.

[22] E. Kusiak-Nejman and A. W. Morawski, "TiO2/graphene-based nanocomposites for water treatment: a brief overview of charge carrier transfer, antimicrobial and photocatalytic performance," *Applied Catalysis B: Environmental*, vol. 253, article S0926337319303777, pp. 179–186, 2019.

[23] A. Toghan and A. Modwi, "Boosting unprecedented indigo carmine dye photodegradation via mesoporous MgO@ g-C3N4 nanocomposite," *Journal of Photochemistry and Photobiology A: Chemistry*, vol. 419, article S1010603021003361, p. 113467, 2021.

[24] A. Modwi, B. Mustafa, M. Ismail et al., "Physicochemical and photocatalytic performance of the synthesized RuO2-ZnO photo-composite in the presence of pectinose solution," *Environmental Nanotechnology, Monitoring & Management*, vol. 15, article 100403, 2021.

[25] H. Van Bao, N. M. Dat, N. T. H. Giang et al., "Behavior of ZnO-doped TiO_2/rGO nanocomposite for water treatment enhancement," *Surfaces and Interfaces*, vol. 23, article S2468023021000274, p. 100950, 2021.

[26] Y. Yu, W. Yan, X. Wang et al., "Surface engineering for extremely enhanced charge separation and photocatalytic hydrogen evolution on g-C3N4," *Advanced Materials*, vol. 30, no. 9, p. 1705060, 2018.

[27] Z. Wu, X. He, Z. Gao, Y. Xue, X. Chen, and L. Zhang, "Synthesis and characterization of Ni-doped anatase TiO 2 loaded on magnetic activated carbon for rapidly removing triphenylmethane dyes," *Environmental Science and Pollution Research*, vol. 28, no. 3, article 10698, pp. 3475–3483, 2021.

[28] E. Vesali-Kermani, A. Habibi-Yangjeh, and S. Ghosh, "Visible-light-induced nitrogen photofixation ability of g-C_3N_4 nanosheets decorated with MgO nanoparticles," *Journal of Industrial and Engineering Chemistry*, vol. 84, article S1226086X20300058, pp. 185–195, 2020.

[29] S. Tanemura, L. Miao, W. Wunderlich et al., "Fabrication and characterization of anatase/rutile–TiO2 thin films by magnetron sputtering: a review," *Science and Technology of Advanced Materials*, vol. 6, no. 1, pp. 11–17, 2005.

[30] D. N. Zhang, L. Zhao, J. F. Wang, and Y. L. Li, "Electronic structures and the stability of MgO surface: density functional study," *Surface Review and Letters*, vol. 22, no. 3, article 1550037, 2015.

[31] S. Datta, P. Singh, D. Jana et al., "Exploring the role of electronic structure on photo-catalytic behavior of carbon-nitride polymorphs," *Carbon*, vol. 168, article S0008622320303316, pp. 125–134, 2020.

[32] F. J. Sotomayor, K. A. Cychosz, and M. Thommes, "Characterization of micro/mesoporous materials by physisorption: concepts and case studies," *Accounts Materials and Surface Research*, vol. 3, no. 2, pp. 34–50, 2018.

[33] C. V. Tran, D. V. Quang, H. P. Nguyen Thi, T. N. Truong, and D. D. la, "Effective removal of Pb (II) from aqueous media by a new design of Cu–Mg binary ferrite," *ACS Omega*, vol. 5, no. 13, pp. 7298–7306, 2020.

[34] M. Kapilashrami, J. Xu, K. V. Rao, L. Belova, E. Carlegrim, and M. Fahlman, "Experimental evidence for ferromagnetism at room temperature in MgO thin films," *Journal of Physics: Condensed Matter*, vol. 22, no. 34, p. 345004, 2010.

[35] L. Ge, Z. Peng, W. Wang et al., "gC 3 N 4/MgO nanosheets: light-independent, metal-poisoning-free catalysts for the activation of hydrogen peroxide to degrade organics," *Journal of Materials Chemistry A*, vol. 6, no. 34, pp. 16421–16429, 2018.

[36] R. K. Schulze, M. A. Hill, R. D. Field, P. A. Papin, R. J. Hanrahan, and D. D. Byler, "Characterization of carbonated serpentine using XPS and TEM," *Energy Conversion and Management*, vol. 45, no. 20, article S0196890404000433, pp. 3169–3179, 2004.

[37] Z. Mao, J. Chen, Y. Yang, D. Wang, L. Bie, and B. D. Fahlman, "Novel g-C3N4/CoO nanocomposites with significantly enhanced visible-light photocatalytic activity for H2 evolution," *ACS Applied Materials & Interfaces*, vol. 9, no. 14, pp. 12427–12435, 2017.

[38] P. Mei, H. Wang, H. Guo et al., "The enhanced photodegradation of bisphenol A by TiO_2/C_3N_4 composites," *Environmental Research*, vol. 182, article S0013935119308862, p. 109090, 2020.

[39] N. Tian, Y. Zhang, X. Li et al., "Precursor-reforming protocol to 3D mesoporous g-C_3N_4 established by ultrathin self-doped nanosheets for superior hydrogen evolution," *Nano Energy*, vol. 38, article S221128551730318X, pp. 72–81, 2017.

[40] K. Sun, M. Kang, Z. Zhang et al., "Impact of deashing treatment on biochar structural properties and potential sorption mechanisms of phenanthrene," *Environmental Science & Technology*, vol. 47, no. 20, pp. 11473–11481, 2013.

[41] H. Lu, W. Zhang, Y. Yang, X. Huang, S. Wang, and R. Qiu, "Relative distribution of Pb^{2+} sorption mechanisms by sludge-derived biochar," *Water Research*, vol. 46, no. 3, article S0043135411007500, pp. 854–862, 2012.

[42] Y.-S. Ho and G. McKay, "Pseudo-second order model for sorption processes," *Process Biochemistry*, vol. 34, no. 5, article S0032959298001125, pp. 451–465, 1999.

[43] A. R. Usman, A. S. Sallam, A. al-Omran et al., "Chemically modified biochar produced from conocarpus wastes: an efficient sorbent for Fe (II) removal from acidic aqueous solutions," *Adsorption Science & Technology*, vol. 31, no. 7, pp. 625–640, 2013.

[44] D. Kołodyńska, R. Wnętrzak, J. J. Leahy, M. H. B. Hayes, W. Kwapiński, and Z. Hubicki, "Kinetic and adsorptive characterization of biochar in metal ions removal," *Chemical Engineering Journal*, vol. 197, article S1385894712005979, pp. 295–305, 2012.

[45] A. Usman, A. Sallam, M. Zhang et al., "Sorption process of date palm biochar for aqueous Cd (II) removal: efficiency and mechanisms," *Water, Air, & Soil Pollution*, vol. 227, no. 12, article 3161, pp. 1–16, 2016.

[46] C. Xiong, W. Wang, F. Tan, F. Luo, J. Chen, and X. Qiao, "Investigation on the efficiency and mechanism of Cd (II) and Pb (II) removal from aqueous solutions using MgO nanoparticles," *Journal of Hazardous Materials*, vol. 299, article S0304389415006275, pp. 664–674, 2015.

[47] N. Kataria and V. Garg, "Optimization of Pb (II) and Cd (II) adsorption onto ZnO nanoflowers using central composite design: isotherms and kinetics modelling," *Journal of Molecular Liquids*, vol. 271, pp. 228–239, 2018.

[48] D. Mohan, H. Kumar, A. Sarswat, M. Alexandre-Franco, and C. U. Pittman Jr., "Cadmium and lead remediation using magnetic oak wood and oak bark fast pyrolysis bio-chars," *Chemical Engineering Journal*, vol. 236, article S1385894713012503, pp. 513–528, 2014.

[49] B. Aissa, L. Khezami, K. Taha et al., "Yttrium oxide-doped ZnO for effective adsorption of basic fuchsin dye: equilibrium, kinetics, and mechanism studies," *International journal of Environmental Science and Technology*, pp. 1–14, 2021.

[50] S. Xu, Z. Zhong, W. Liu, H. Deng, and Z. Lin, "Removal of Sb (III) from wastewater by magnesium oxide and the related mechanisms," *Environmental Research*, vol. 186, article S0013935120303820, p. 109489, 2020.

[51] B. Priyono, A. Z. Syahrial, A. H. Yuwono, E. Kartini, M. Marfelly, and W. M. F. Rahmatulloh, "Synthesis of lithium titanate (Li4Ti5O12) through hydrothermal process by using lithium hydroxide (LiOH) and titanium dioxide (TiO2) xerogel," *International Journal of Technology*, vol. 6, no. 4, pp. 555–564, 2015.

[52] Y. Feng, G. Chen, Y. Zhang et al., "Superhigh co-adsorption of tetracycline and copper by the ultrathin g-C_3N_4 modified graphene oxide hydrogels," *Journal of Hazardous Materials*, vol. 424, no. Part B, article 127362, Article ID S030438942102330X, 2022.

[53] C. Shen, C. Chen, T. Wen, Z. Zhao, X. Wang, and A. Xu, "Superior adsorption capacity of g-C_3N_4 for heavy metal ions from aqueous solutions," *Journal of Colloid and Interface Science*, vol. 456, article S0021979715005354, pp. 7–14, 2015.

[54] H. Wang, Y. Lin, Y. Li et al., "A novel magnetic Cd (II) ion-imprinted polymer as a selective sorbent for the removal of cadmium ions from aqueous solution," *Journal of Inorganic and Organometallic Polymers and Materials*, vol. 29, no. 6, article 1148, pp. 1874–1885, 2019.

[55] X. Yuan, W. Xia, J. An et al., "Removal of Cd (II) ion from aqueous solution by adsorption on wasted low grade phosphorus-containing iron ore," in *8th International Symposium on High-Temperature Metallurgical Processing*, pp. 779–787, Springer, Cham, 2017.

[56] W. Liao, D. Bao, H. Q. Li, and P. Yang, "Cu (II) and Cd (II) removal from aqueous solution with LDH@ GO-NH2 and LDH@ GO-SH: kinetics and probable mechanism," *Environmental Science and Pollution Research*, vol. 28, no. 46, article 15558, pp. 65848–65861, 2021.

[57] L. Sun, J. Wang, J. Wu et al., "Constructing nanostructured silicates on diatomite for Pb (II) and Cd (II) removal," *Journal of Materials Science*, vol. 54, no. 9, article 3388, pp. 6882–6894, 2019.

[58] S. Wang, D. Zhou, J. Zhou, C. Liu, X. Xiao, and C. Song, "Cd (II) removal by novel fabricated ground calcium carbonate/nano-TiO2 (GCC/TiO2) composite from aqueous solution,"

Water, Air, & Soil Pollution, vol. 230, no. 7, article 4205, pp. 1–14, 2019.

[59] J. Zhang and F. Xie, "Effects of Mn(II) addition on Cd(II) removal by hydrated manganese dioxide," *Environmental Science and Pollution Research*, vol. 29, no. 24, article 18381, pp. 36295–36312, 2022.